*Article*

**aeroacoustics**

*International Journal of Aeroacoustics*
2017, Vol. 16(7–8) 603–625

DOI: 10.1177/1475472X17727606
journals.sagepub.com/home/jae

SAGE

# Numerical study of the flow and the near acoustic fields of an underexpanded round free jet generating two screech tones

**Romain Gojon and Christophe Bogey**

**Abstract**

The flow and near acoustic fields of a supersonic round free jet are explored using a compressible large eddy simulation. At the exit of a straight pipe nozzle, the jet is underexpanded, and is characterized by a Nozzle Pressure Ratio of 4.03 and a Temperature Ratio of 1. It has a fully expanded Mach number of 1.56, an exit Mach number of 1, and a Reynolds number of $6\times10^4$. Flow snapshots, mean flow fields and convection velocity in the jet shear layers are consistent with experimental data and theoretical results. Furthermore, two screech tones are found to emerge in the pressure spectrum calculated close to the nozzle. Using a Fourier decomposition of the pressure fields, the two screech tones are found to be associated with anticlockwise helical oscillation modes. Besides, the frequencies of the screech tones and the associated oscillation modes both agree with theoretical predictions and measurements. Moreover, pressure fields filtered at the screech frequencies reveal the presence of hydrodynamic-acoustic standing waves. In those waves, the regions of highest amplitude in the jet are located in the fifth and the sixth cells of the shock cell structure. The two screech tones therefore seem to be linked to two different loops established between the nozzle and the fifth and sixth shock cells, respectively. In the pressure fields, three other acoustic components, namely the low-frequency mixing noise, the high-frequency mixing noise and the broadband shock-associated noise, are noted. The directivity and frequency of the mixing noise are in line with numerical and experimental studies. A production mechanism of the mixing noise consisting of sudden intrusions of turbulent structures into the potential core is discussed. Then, the broadband shock-associated noise is studied. This noise component is due to the interactions between the turbulent structure in the shear layers and the shocks in the jet. By analyzing the near pressure fields, this noise component is found to be produced mainly in the sixth shock cell. Finally, using the size of this shock cell in the

Laboratoire de Mécanique des Fluides et d'Acoustique, UMR CNRS 5509, Ecole Centrale de Lyon, Université de Lyon, Ecully Cedex, France

**Corresponding author:**
Romain Gojon, Laboratoire de Mécanique des Fluides et d'Acoustique, UMR CNRS 5509, Ecole Centrale de Lyon, Université de Lyon, 69134 Ecully Cedex, France.
Email: romain.gojon@ec-lyon.fr

classical theoretical model of this noise component, a good agreement is found with the simulation results.

**Keywords**
Large eddy simulation, supersonic jet, screech

Date received: 9 September 2016; accepted: 1 June 2017

## Introduction

In non-ideally expanded supersonic jets, several acoustic components including screech noise, mixing noise and broadband shock-associated noise are observed. The screech noise is due to an aeroacoustic feedback mechanism established between the turbulent structures propagating downstream and the acoustic waves propagating upstream. This mechanism was described by Powell,[1] then by Raman,[2] who proposed that the turbulent structures developing in the jet shear layers and propagating in the downstream direction interact with the quasi-periodic shock cell structure of the jet, creating upstream propagating acoustic waves. The resonant loop is closed at the nozzle lips where sound waves are reflected back and excite the shear layers. Moreover, for round jets, Powell[1] identified four modes, labeled $A$, $B$, $C$, and $D$, on the basis of the screech frequency evolution with the ideally expanded Mach number $\mathcal{M}_j$. Each mode is dominant for a specific ideally expanded Mach number range and frequency jumps are noted between the modes. Later, Merle[3] showed that mode $A$ can be divided into modes $A1$ and $A2$. Davies and Oldfield[4] studied the oscillation modes of the jets associated with the five screech modes. They found that $A1$ and $A2$ modes are linked to axisymmetric oscillation modes of the jet, $B$ to sinuous and sometimes helical modes, $C$ to helical modes and $D$ to sinuous modes. Mixing noise is observed in both subsonic[5] and supersonic[6] jets. The dominant Strouhal number of this noise component is around 0.2 and its directivity is well marked around angles of 20° with respect to the downstream direction. This component is mainly generated at the end of the potential core.[7,8,9] For subsonic jets, Bogey et al.[10] and Bogey and Bailly[7] proposed that this acoustic component is due to the intermittent intrusion of turbulent structures into the potential core. The broadband shock-associated noise is produced by the interactions between the turbulence and the shock cell structure. Martlew[11] was the first to clearly identify this noise. Its central frequency varies with the angle in the far field, according to experiments.[12–14] Harper-Bourne and Fisher[15] proposed a model which permits to predict the central frequency of this noise component as a function of the observation angle.

In the present work, the LES of a round supersonic underexpanded jet is carried out in order to investigate the acoustic mechanisms in non-ideally expanded jets. The jet corresponds to the reference free jet in a study on impinging jets performed by Gojon et al.[16] The results from this jet were also used to generate schlieren-like images, in a study of Castelain et al.,[17] in order to asses the quality of the estimation of the convection velocity in the jet shear layers using schlieren pictures in experiments. In the present paper, the spectral and hydrodynamic properties of the jet are described and compared with experimental data and models. Three acoustic components, namely the screech noise, the mixing noise, and the broadband shock-associated noise, are investigated. In particular, two screech tones are found in the spectra calculated in the vicinity of the nozzle. The causes of such a result

are sought. The production mechanism of the mixing noise is then investigated by evaluating skewness and kurtosis factors of the fluctuating pressure. Finally, the broadband shock-associated noise is examined. Notably, a discussion about the lengthscale to use in the classical model of this noise component is conducted. The paper is organized as follows. The jet parameters and the numerical methods used for the LES are given in the Parameters section. The aerodynamic results are analyzed in the Aerodynamic results section, and the acoustic mechanisms are investigated in the Acoustic results section. Concluding remarks are provided in the last section.

## Parameters

### Jets parameters

The large-eddy simulation of a round supersonic jet is performed. The jet originates from a straight pipe nozzle of radius $r_0$, whose lip is $0.1r_0$ thick. The jet is underexpanded, and has a Nozzle Pressure Ratio of $NPR = P_r/P_{amb} = 4.03$ and a Temperature Ratio $TR = T_r/T_{amb} = 1$, where $P_r$ and $T_r$ are the stagnation pressure and temperature and $P_{amb}$ and $T_{amb}$ are the ambient values. As for a jet generated by a convergent nozzle, the exit Mach number of the present jet is $\mathcal{M}_e = u_e/c_e = 1$, where $u_e$ and $c_e$ are the velocity and speed of sound in the jet. Moreover, the jet is characterized by a fully expanded Mach number of $\mathcal{M}_j = u_j/c_j = 1.56$, where $u_j$ and $c_j$ are the velocity and the speed of sound in the ideally expanded equivalent jet. Its Reynolds number is $Re_j = u_j D_j/\nu = 6 \times 10^4$, where $D_j$ is the nozzle diameter of the ideally expanded equivalent jet and $\nu$ is the kinematic molecular viscosity. At the nozzle inlet, a Blasius boundary-layer profile with a thickness of $0.15r_0$ and a Crocco-Busemann profile are imposed for velocity and density. The exit conditions of the jet and the nozzle lip thickness are similar to those in the experiments of Henderson et al.[18] Finally, low-amplitude vortical disturbances, not correlated in the azimuthal direction,[19] are added in the boundary layer in the nozzle, at $z = -0.5r_0$, in order to generate velocity fluctuations at the nozzle exit. The strength of the forcing is chosen in order to obtain turbulent intensities of around 6% of the fully expanded jet velocity at the nozzle exit.

### Numerical parameters

The LES is performed by solving the unsteady compressible Navier–Stokes equations on a cylindrical mesh $(r, \theta, z)$. An explicit six-stage Runge–Kutta algorithm and low-dispersion and low-dissipation explicit eleven-point finite differences are used for time integration and spatial derivation,[20,21] respectively. At the end of each time step, a high-order filtering is applied to the flow variables in order to remove grid-to-grid oscillations and to dissipate subgrid-scale turbulent energy. The filtering thus acts as a subgrid scale model.[22–25] The radiation conditions of Tam and Dong[26] are implemented at the boundaries of the computational domain. A sponge zone combining grid stretching and Laplacian filtering is also employed to damp the turbulent fluctuations before they reach the boundaries. Moreover, non-slip adiabatic conditions are used to simulate the nozzle walls. In order to increase the time step of the simulation, the effective resolution near the origin of the cylindrical coordinates is reduced.[27] The axis singularity is treated with the method of Mohseni and Colonius.[28] Finally, a shock-capturing filtering is used in order to avoid Gibbs oscillations near shocks. It consists in applying a conservative second-order filter at a

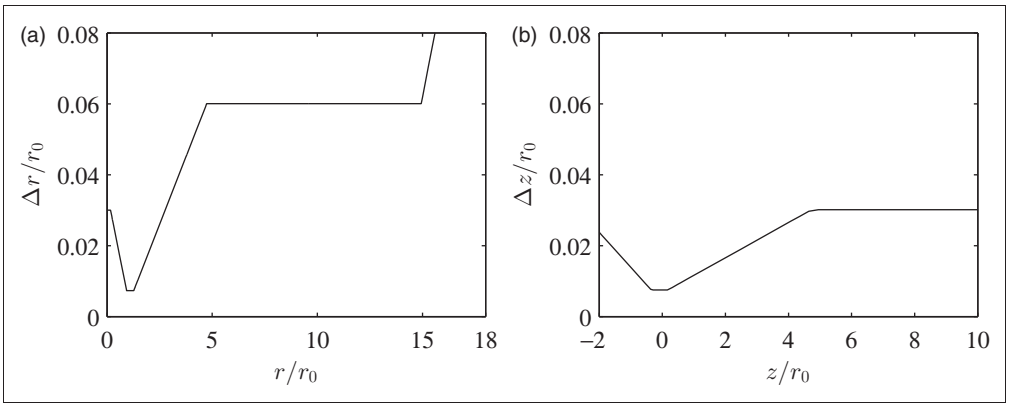


**Figure 1.** Representation of (a) the radial mesh spacings, and (b) the axial mesh spacings.

magnitude determined each time step using a shock sensor.[29] It was successfully used by Cacqueray et al.[30] for the LES of an overexpanded jet at an equivalent Mach number of $\mathcal{M}_j = 3.3$.

The simulation is carried out using an OpenMP-based in-house solver, and a total of 250, 000 iterations are computed during the steady state. The temporal discretization is set to $\Delta t = 0.002 D_j/u_j$, permitting a simulation time of $500 D_j/u_j$. The cylindrical mesh contains $(n_r, n_\theta, n_z) = (500, 512, 1565) \simeq 400$ million points. The variations of the radial and the axial mesh spacings are represented in Figure 1. In Figure 1(a), the minimal axial mesh spacing is located in the jet shear layer, at $r = r_0$, and is equal to $\Delta r = 0.0075 r_0$. Farther from the jet axis, the mesh is stretched to reach the maximum value of $\Delta r = 0.06 r_0$ for $5r_0 \leq r \leq 15r_0$. For $r \geq 15r_0$, a sponge zone is implemented. In Figure 1(b), the minimal axial mesh spacing is found at the nozzle lips, at $z = 0$, and is equal to $\Delta z = 0.0075 r_0$. Farther downstream, the mesh is stretched, leading to $\Delta z = 0.03 r_0$ for $5r_0 \leq z \leq 30r_0$. For $z > 30r_0$, a sponge zone is applied. In the physical domain the grid is stretched at rates lower than 1%, in order to preserve numerical accuracy. The maximum mesh spacing of $0.06 r_0$ in the physical domain allows acoustic waves with Strouhal numbers up to $St = f D_j/u_j = 5.3$ to be well propagated, where $f$ is the frequency. Finally, note that a similar mesh is used in a convergence study made in a previous study for the LES of an initially highly disturbed high-subsonic jet.[19]

## Aerodynamic results

### *Flow snapshots*

Three-dimensional views of the jet are displayed in Figure 2. In the top figure, isosurfaces of density are displayed in order to show the shock-cell structure. The boundaries of the mixing layer are also represented using isosurfaces of density. The bottom figure provides a zoomed view of the nozzle exit region. Longitudinal structures appear on the outer boundary of the first shock cell. The temporal stability of these structures can be seen in the corresponding movie "Movie 2", available online at http://acoustique.ec-lyon.fr/publi/gojon_ija17_movie2.avi. Such structures have been described in several experiments, including those by Arnette et al.[31] They are due to the small perturbations at the nozzle exit which are amplified by

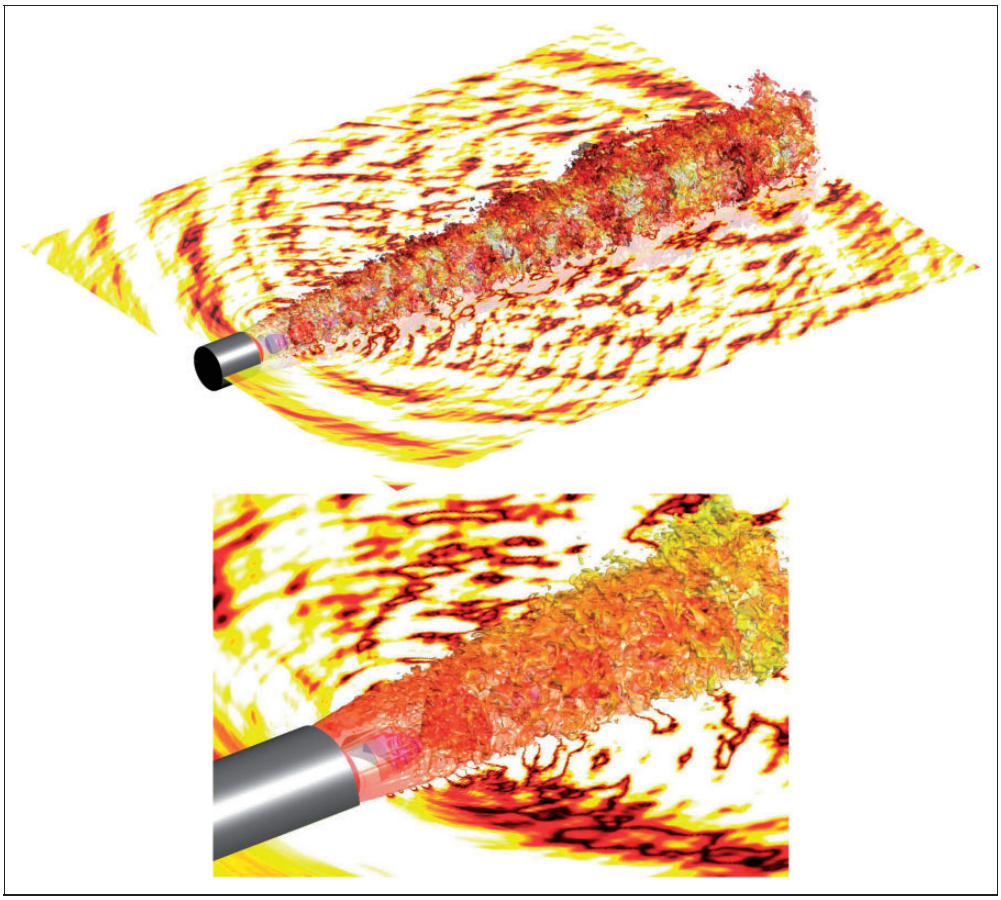

**Figure 2.** Isosurfaces of density: in purple and red for values of 0.8 and 2.5 kg.m$^{-3}$, colored by the local Mach number in the top view and by the radial position in the bottom view for the value 1.25 kg.m$^{-3}$. The pressure field at $\theta = 0$ and $\pi$ is also shown with a color scale ranging from $-2000$ to 2000 Pa for the pressure, from white to red. The nozzle is in grey. For the bottom view, a movie is available online at http://acoustique.ec-lyon.fr/publi/gojon_ija17_movie2.avi

Taylor–Goertler-type instabilities, and are specific to underexpanded jets. Finally, in the two figures, the pressure field obtained in the planes $\theta = 0$ and $\pi$ is added in order to show the near acoustic fields of the jet. Notably, an acoustic component propagating in the upstream direction is visible in the vicinity of the nozzle.

In order to illustrate the jet flow development, a snapshot of the vorticity norm obtained in the plane $(z, r)$ is presented in Figure 3. The shear layer develops rapidly downstream of the nozzle exit with both small and large turbulent structures, in agreement with the Reynolds number $Re_j$ of $6 \times 10^4$. The end of the jet potential core appears to be located around $15r_0$. An empirical model was proposed by Lau et al.[32] to predict the length of the potential core $z_p$ for isothermal jets with Mach number up to 2.5. Later, Tam et al.[33] included in that model the temperature ratio between the exit and ambient temperatures

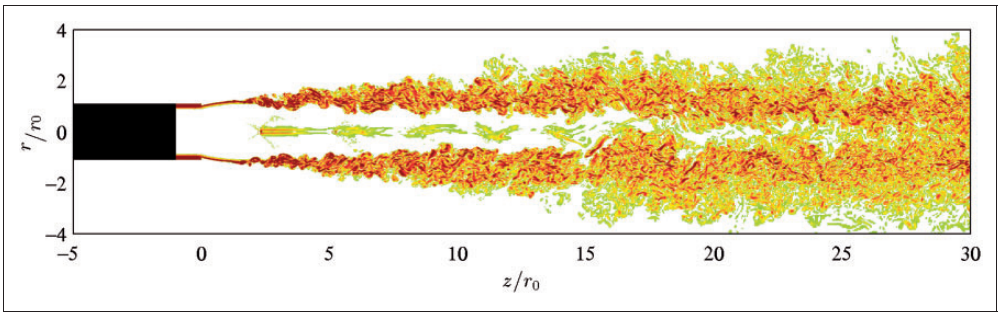


**Figure 3.** Snapshot of the vorticity norm $|\omega|$ obtained in the ($z$, $r$) plane. The colour scale ranges up to the level of $10u_j/D_j$, from white to red. The nozzle is in black.

in order to take into account compressibility effects. For the present jet, where the exit temperature $T_e$ is lower than the ambient temperature $T_{amb}$, the model can be written

$$\frac{z_p}{D_j} = 4.2 + 1.1\mathcal{M}_j^2 + 1.1\left(1 - \frac{T_e}{T_{amb}}\right) \tag{1}$$

For the present jet, equation (1) yields $z_p = 15.6r_0$, which is in good agreement with the result of the simulation.

A snapshot of the density and fluctuating pressure obtained in the ($z$, $r$) plane is provided in Figure 4(a). A movie, labeled "Movie 1", showing the temporal evolution of the jet is also available online at http://acoustique.ec-lyon.fr/publi/gojon_ija17_movie1.avi. A shock-cell structure, typical of an underexpanded jet, is observed in the density field. It contains around 10 shock cells. Because the jet is strongly underexpanded with a $NPR$ of 4.03, a Mach disk is found in the first cell, at $z = 2.35r_0$. This is in agreement with the results of Powell,[34] Henderson,[35] and Addy,[36] who noted that a Mach disk is generated in underexpanded jets for $NPR > 3.8$ or 3.9. For the comparison, a Schlieren picture of an underexpanded jet obtained by André et al.[37] is displayed in Figure 4(b). The fully expanded Mach number of the jet is $\mathcal{M}_j = 1.55$ and the exit Mach number is $\mathcal{M}_e = 1$. A strong similarity appears with notably the presence of a Mach disk in the first cell. In the pressure field, in Figure 4(a), two acoustic contributions appear. First, circular wavefronts seem to originate from the first five cells. They are due to the interactions between the shocks and the turbulence in the shear layers. Upstream propagating acoustic waves are also observed in the vicinity of the nozzle.

## Mean fields

The mean axial and radial velocity fields of the jet are presented in Figure 5, where the experimental PIV results of André et al.[37] are also displayed for a $\mathcal{M}_j = 1.5$ and $\mathcal{M}_e = 1$ jet. The shock-cell structure and the levels obtained in the LES and in the experiment are in good agreement. The mean total velocity field in the ($z$, $r$) plane is shown in Figure 6. It compares very well with the experimental results of Henderson et al.[18] for a jet with similar exit conditions.

In Figures 5 and 6, the length $L_s$ of the first shock cell of the jet is approximately $3.20r_0$. This result is identical to those obtained by André et al.[37] and of Henderson et al.[18] for

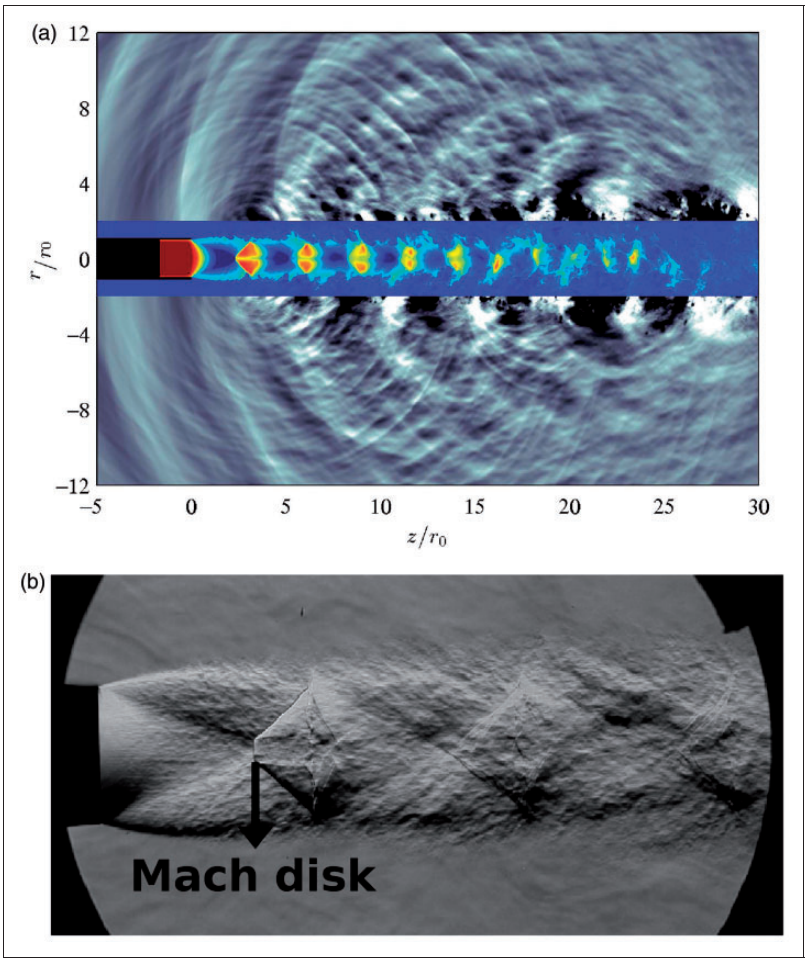


**Figure 4.** (a) Snapshot of the density in the jet and of the fluctuating pressure. The colour scale ranges from 1 to 3 kg.m$^{-3}$ for the density, from blue to red, and from –2000 to 2000 Pa for the pressure, from white to black; (b) Schlieren picture of an underexpanded jet obtained by André et al.[37] for a $\mathcal{M}_j = 1.55$ and $\mathcal{M}_e = 1$ jet; a movie is available online at http://acoustique.ec-lyon.fr/publi/gojon_ija17_movie1.avi

similar jets. Moreover, this length can be estimated by using a first-order shock solution based on the pressure ratio $p_s/p_a$, where $p_s$ is the pressure perturbation of the shock-cell structure and $p_s + p_a$ is the pressure in the jet. This model was proposed by Prandtl[38] in 1904. Later, the following approximated solution was given by Pack[39]

$$L_s \simeq 1.22\beta D_j \tag{2}$$

where $\beta = \sqrt{\mathcal{M}_j^2 - 1}$. For the present jet, equation (2) provides $L_s = 3.20r_0$, which is identical to the value reported above.

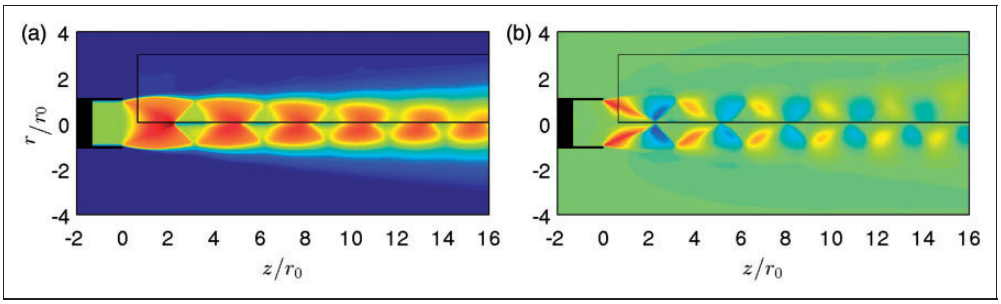


**Figure 5.** Mean fields for (a) the axial and (b) the radial velocities. The colour scale ranges from 0 to 600 m.s$^{-1}$ for the axial velocity, from blue to red, and from $-150$ to 150 m.s$^{-1}$ for the radial velocity, from blue to red; the PIV results of André et al.[37] for a $\mathcal{M}_j = 1.5$ and $\mathcal{M}_e = 1$ jet are displayed in the black rectangles.

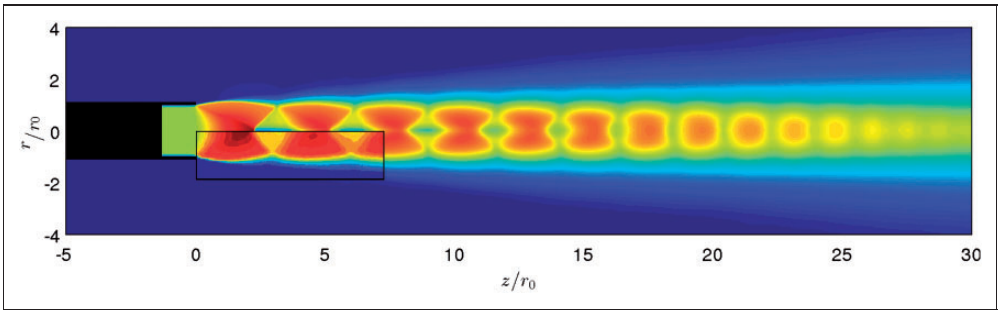


**Figure 6.** Mean total velocity field with a colour scale ranging from 0 to 600 m.s$^{-1}$, from blue to red; the PIV results of Henderson et al.[18] for a jet with similar exit conditions are displayed in the black rectangle.

The shock-cell size decreases with the downstream distance as shown in Figure 5(a). This trend is due to the growth of the shear layer and to the dissipation of the shock-cell structure by the turbulence.[33] The normalized shock-cell sizes in the present jet and in several underexpanded jets of André et al.[37] are presented in Figure 7. A good agreement is found between the simulation and the experiments. Moreover, the variation of the shock-cell size appears to behave linearly. Such evolution was noted by Harper-Bourne and Fisher[15] who proposed the following relation for the size of the $n$-th cell of the structure

$$L_n = L_s - (n-1)\Delta L \tag{3}$$

where $\Delta L$ is the variation of the cell size from one cell to another. The results obtained for the simulated jet yield $\Delta L/L_s = 5\%$. Experimentally, for underexpanded supersonic jets, Harper-Bourne and Fisher[15] and André et al.[37] found $\Delta L/L_s = 6\%$ and $\Delta L/L_s = 3\%$, respectively. The lower value in the experiment of André et al.[37] may be due to the presence of a secondary flow at a Mach number of $\mathcal{M} = 0.05$.

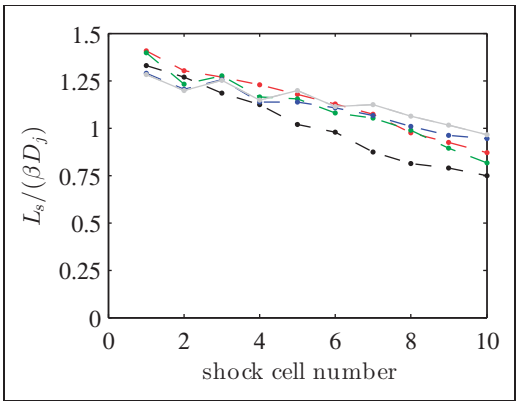


**Figure 7.** Normalized lengths of the first 10 shock cells obtained for – • – the present jet, and the experimental jets of André et al.[37] with – • – $\mathcal{M}_j = 1.50$, – • – $\mathcal{M}_j = 1.35$, – • – $\mathcal{M}_j = 1.15$ and – • – $\mathcal{M}_j = 1.10$.

Finally, the Mach disk located at $z_M = 2.3r_0$ is a normal shock. For such shocks, the Rankine–Hugoniot jump condition yields

$$\frac{u_2}{u_1} = \frac{(\gamma - 1)\mathcal{M}_1^2 + 2}{(\gamma + 1)\mathcal{M}_1^2} \tag{4}$$

where $u_1$ and $u_2$ are the velocities upstream and downstream of the normal shock, respectively, and $\mathcal{M}_1$ is the upstream Mach number. In the present jet, the simulation provides $u_1 = 595$ m.s$^{-1}$ and $\mathcal{M}_1 = 2.75$ before the Mach disk and $u_2 = 166$ m.s$^{-1}$ after the Mach disk. The latter value compares very well with the value $u_{2_{RH}} = 164$ m.s$^{-1}$ predicted by equation (4). The Mach disk position $z_M$ and diameter $D_M$ can be estimated from the mean velocity field, yielding $z_M = 2.3r_0$ and $D_M = 0.25r_0$. Experimentally, for jets with a $NPR$ exceeding 3.9, Addy[36] proposed the following empirical expressions

$$\frac{z_M}{D_j} = 0.65\sqrt{NPR} \tag{5}$$

$$\frac{D_M}{D_j} = 0.36\sqrt{NPR} - 3.9 \tag{6}$$

The Mach disk positions and diameters obtained from the present simulation, the experiments of Addy[36] and expressions (5) and (6), are plotted as a function of the Nozzle Pressure Ratio in Figure 8. A good overall agreement is found. It can be noted that expression (5) slightly overestimates the position of the Mach disk for $NPR < 6$.

## *Velocity fluctuations*

The rms values of axial and radial velocity fluctuations obtained for the present jet are represented in Figure 9, where the experimental PIV results of André et al.[37] are also shown. The results obtained in the LES and in the experiment are in fairly good agreement. For the axial velocity, the amplitude appears to oscillate in the jet shear layer according to

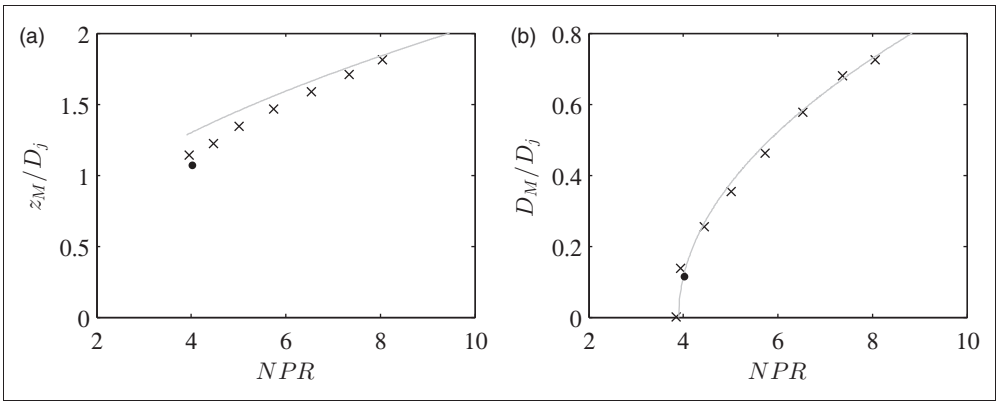


**Figure 8.** (a) Position and (d) diameter of the Mach disk at the end of the first shock cell obtained • in the present jet, × in the experiment of Addy,[36] and —— using expressions (5) and (6).

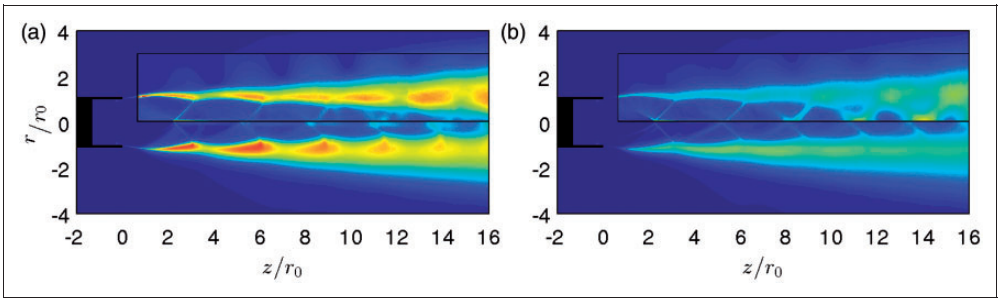


**Figure 9.** Rms values for the (a) axial and (b) radial velocities in the present jet. The colour scale ranges from 0 to 100 m.s$^{-1}$, from blue to red; the PIV results of André et al.[37] for a $\mathcal{M}_j = 1.5$ and $\mathcal{M}_e = 1$ jet are shown in the black rectangles.

the shock cell structure. On the contrary, for the radial velocity, the amplitude in the jet shear layer does not vary significantly. Moreover, the jet shear layer is thicker in the LES than in the experiment. This result may be due to the higher Reynolds number in the experiment ($Re_j = 1 \times 10^6$) than in the simulation ($Re_j = 6 \times 10^4$).

The peak rms values of velocity fluctuations in the jet shear layer are represented in Figure 10 as a function of the axial distance. In Figure 10(a), the peak rms value of axial velocity fluctuations varies following the shock cell structure. In a given cell, it increases gradually and then decreases rapidly on the cell ending. For example, in the first cell, it increases up to $z = 3r_0$, where it is equal to 18% of the equivalent fully expanded jet velocity in the simulated jet and 16% in the experimental jet. A rapid decrease is visible downstream, where values of 13.5% and 12.5% are reached in the beginning of the next cell, respectively. In Figure 10(b), the peak rms value of radial velocity fluctuations is almost uniform in the simulated jet, and is equal to 11%. In the experimental jet, this value is about 8% in the first three cells of the shock cell structure. Farther downstream, for $z \geq 10$, the peak rms value of

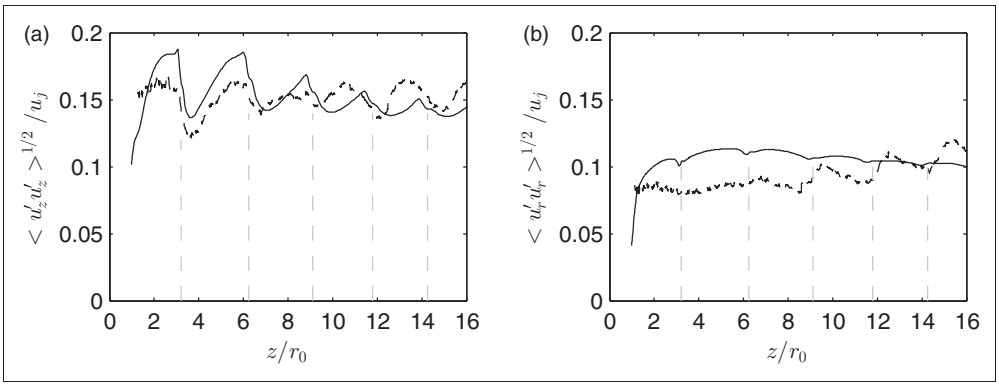


**Figure 10.** Peak rms values of (a) axial and (b) radial velocity fluctuations as a function of the axial position; —— simulation results and – – – PIV results of André et al.[37] for a $\mathcal{M}_j = 1.5$ and $\mathcal{M}_e = 1$ jet. The dashed vertical grey lines indicate the end of the cells in the shock-cell structure of the simulated jet.

radial velocity fluctuations varies according to the shock cell structure in the experimental jet.

### *Convection velocity*

The local convection velocity of the turbulent structures is estimated at the center of the shear layer, where the velocity fluctuations are maximum, as presented in Figure 11. It is calculated from cross-correlations of axial velocity fluctuations between two points located at $z \pm 0.1r_0$.

The local convection velocity obtained in the present jet is presented in Figure 12 as a function of the axial direction. It is not constant but varies according to the shock-cell structure, as observed experimentally by André[12] for round underexpanded jets. In the first cell, for example, the convection velocity increases from the value $u_c = 0.4u_j$ up to the value $0.63u_j$, as the velocity inside the jet increases. Farther downstream, the convection velocity decreases down to the value of $0.60u_j$, following the decrease of the velocity inside the jet due to the presence of a Mach disk and of an oblique annular shock. Similar variations are found for the other cells of the shock cell structure. Furthermore, the convection velocity is close to the value $0.35u_j \simeq 0.5u_e$ at the nozzle exit, as expected for instabilities initially growing in the mixing layers just downstream of the nozzle. Moreover, the convection velocity tends to the value $u_c = 0.65u_j$ several radii downstream of the nozzle. This result is in agreement with the experimental results of Harper-Bourne and Fisher,[15] who found a convection velocity of $u_c \simeq 0.70u_j$ for underexpanded supersonic jets using a crossed beam schlieren technique.

## Acoustic results

### *Acoustic spectrum near the nozzle exit*

The pressure spectrum obtained near the nozzle exit at $z = 0$ and $r = 2r_0$ is displayed in Figure 13 as a function of the Strouhal number $St = fD_j/u_j$. Two tones emerge 15 dB above

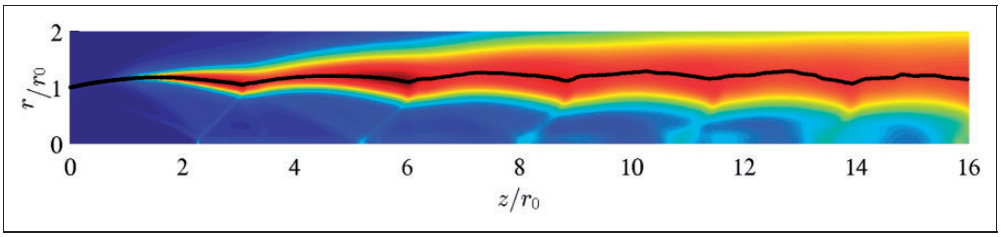


**Figure 11.** Rms values of velocity fluctuations for the simulated jet with a color scale ranging from 0 to 100 m.s$^{-1}$, from blue to red; the black line shows the position of the maximum values.

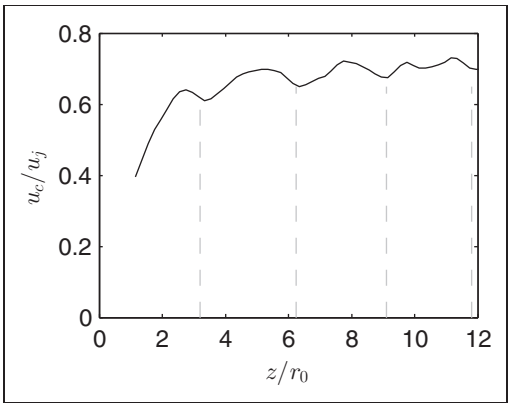


**Figure 12.** Convection velocity of the turbulent structures in the jet shear layers as a function of the axial position. The dashed vertical grey lines indicate the end of the cells in the shock-cell structure.

the broadband noise at Strouhal numbers $St_1 = 0.28$ and $St_2 = 0.305$. Such a result is typical of a screeching jet, see for instance in Westley and Wooley,[40] Panda,[41] and André.[12] The tones at $St_1 = 0.28$ and $St_2 = 0.305$ can therefore be attributed to the generation of screech noise by the jet. For a similar underexpanded jet characterized by $\mathcal{M}_j = 1.55$, $\mathcal{M}_e = 1$ and $Re_j = 1 \times 10^6$, André[12] similarly found two screech tones at Strouhal numbers $St = 0.26$ and $St = 0.29$. The amplitude of the screech tones depends on the nozzle lip thickness, as noted by Raman,[42] but the frequency does not. Thus, the difference in nozzle lip thickness between the present jet and the experimental study of André[12] is unlikely to explain the discrepancy in screech tone frequencies. The difference between the simulation and the experiment can be attributed to the different total jet temperatures. Indeed, in the LES, the total temperature is $T_r = 293K$, whereas in the experiment of André,[12] the total temperature is $T_r = 373K$. A relation for the screech frequency as a function of the total temperature has been proposed by Tam et al.[13] For a mean convection velocity of $< u_c > = 0.65u_j$, the relation is written

$$St = \frac{0.62}{(\mathcal{M}_j^2 - 1)^{1/2}} \left[ 1 + 0.65\mathcal{M}_j \left( 1 + \frac{\gamma - 1}{2} \mathcal{M}_j^2 \right)^{-1/2} \left( \frac{T_0}{T_r} \right)^{-1/2} \right]^{-1} \tag{7}$$

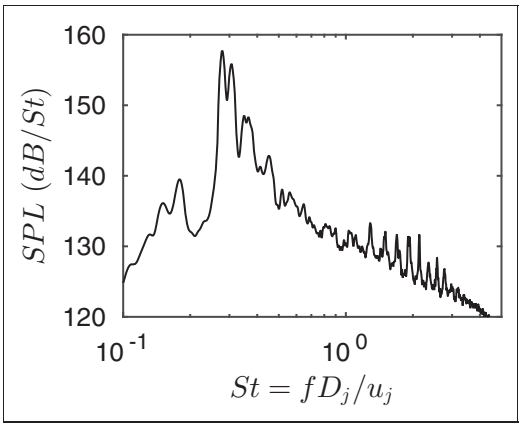


**Figure 13.** Pressure spectrum at $r = 2r_0$ and $z = 0$ as a function of the Strouhal number.

Equation (7) gives $St = 0.285$ for the simulated jet and $St = 0.265$ for the experimental jet, supporting that the difference in screech frequencies between the LES and the experiment is related to the total temperature of the jet.

In order to determine whether the jet products alternatively or simultaneously the two screech tones obtained in the spectrum of Figure 13, a Fast Fourier transform is applied using a sliding window in time, of size $35u_j/D_j$. The result is displayed in Figure 14(a) where the sound pressure level is represented as a function of time $tu_j/D_j$ and Strouhal number. The two screech frequencies at $St_1 = 0.28$ and $St_2 = 0.305$ are visible but their amplitudes vary in time. The sound pressure levels obtained for the two screech tones are shown in Figure 14(b) as a function of time. The intensities of the two tones oscillate between 125 dB/St and 135 dB/St. Moreover, it appears that when the intensity of one screech tone is weak, the intensity of the other tone is strong. A switch between these two tones is thus observed. For non-ideally expanded jets exiting from a rectangular nozzle with a single-bevelled exit, Raman[43] also observed two screech tones switching in time.

## *Fluctuating pressure in the jet*

The pressure fields in the ($z$, $r$) plane have been recorded every 50th time step. A Fourier transform then is applied on each point of the ($z$, $r$) plane. In this way, for a given frequency, the amplitude and the phase fields can be shown. For the screech tones at $St_1 = 0.28$ and $St_2 = 0.305$, they are given in Figure 15. The amplitude fields in Figure 15(a) and (c) exhibit different cell structures. The structures are due to the formation of hydrodynamic-acoustic standing waves. Such waves were previously observed in supersonic screeching jets experimentally by Panda[41] by examining the root-mean-square values of pressure fluctuations in the near field and numerically by Gojon and Bogey.[44] They were also observed by Gojon et al.[45] and Bogey and Gojon[46] in ideally-expanded impinging jets by applying Fourier decomposition to the mean pressure fields and looking at the amplitude fields at the tone frequencies. The cell lengths in these structures are equal to the wavelengths $L_{sw}$ of the standing waves formed between the downstream propagating hydrodynamic waves and

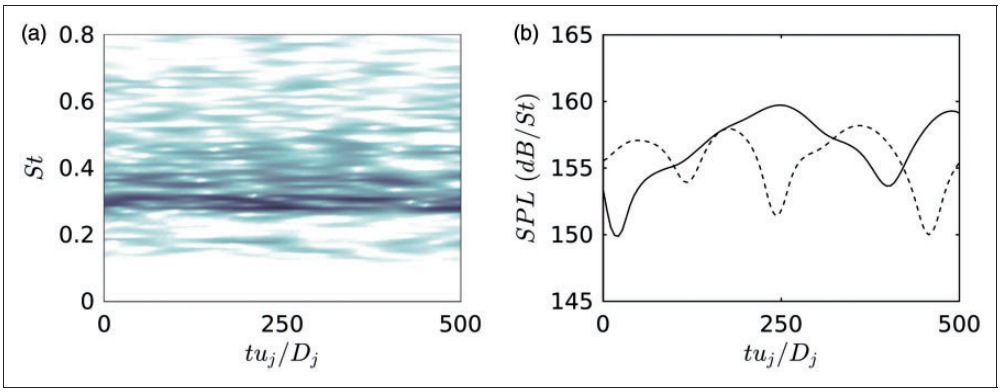


**Figure 14.** (a) Sound pressure level at $r = 2r_0$ and $z = 0$ as a function of time and of Strouhal number and (b) sound pressure levels at $r = 2r_0$ and $z = 0$ as a function of the time for the screech tones —— at $St_1 = 0.28$ and – – – at $St_2 = 0.305$. The color scale ranges from 145 to 165 dB/St.

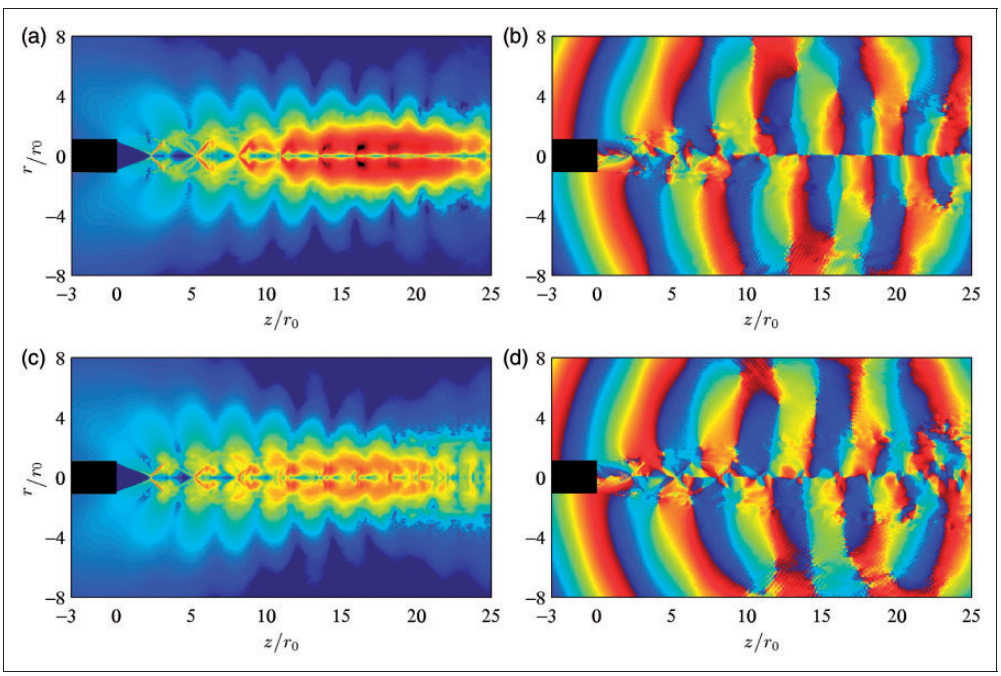


**Figure 15.** Amplitude (left) and phase (right) fields of fluctuating pressure obtained in the (z, r) plane at the two screech tone frequencies of the simulated jet at (a,b) $St_1 = 0.28$ and (c,d) $St_2 = 0.305$. The colour scales range from 120 to 160 dB/St for the amplitude fields and from $-\pi$ to $\pi$ for the phase fields.

the upstream propagating acoustic waves in the jet shear layers. The screech frequencies $f_s$ associated with these wavelengths are provided by the model of Panda.[41]

$$f_s = \frac{< u_c >}{L_{sw}(1 + < u_c > / c_{amb})} \tag{8}$$

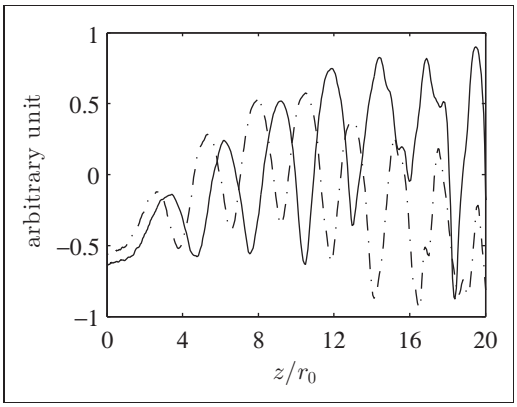


**Figure 16.** Amplitudes of fluctuating pressure obtained along the line $r = 3r_0$ —— at $St_1 = 0.28$ and – – – at $St_2 = 0.305$.

where $< u_c >$ is the mean convection velocity of the structures in the shear layers and $c_{amb}$ is the ambient sound speed.

The amplitudes of pressure fluctuations obtained along the line $r = 3r_0$ at the tone frequencies $St_1 = 0.28$ and $St_2 = 0.305$ are represented in Figure 16. They show oscillations, related to the cell structures visible in Figure 15(a) and (c). The wavelengths of these structures are constant from the second to the fourth cell, for $5r_0 < z < 15r_0$. This result is consistent with the convection velocity remaining almost constant in this region, see in Figure 12. Indeed, using the model of Panda,[41] if the convection velocity is constant, the wavelength $L_{sw}$ will also be constant. Finally, the wavelengths of the cell structures are equal to $L_{sw} \simeq 2.85r_0$ for $St_1 = 0.28$ and $L_{sw} \simeq 2.6r_0$ for $St_2 = 0.305$. In order to apply equation (8) to the simulated jet, the mean convection velocity is considered equal to $< u_c > = 0.65u_j$ in the region $5r_0 < z < 15r_0$, as suggested in Figure 12. Strouhal numbers of $St_s = f_s D_j/u_j \simeq 0.275$ for $L_{sw} \simeq 2.85r_0$ and $St_s = f_s D_j/u_j \simeq 0.30$ for $L_{sw} \simeq 2.6r_0$ are thus found. The values are in agreement with the two screech tones obtained in Figure 13. Moreover, in the amplitude fields of Figure 15(a) and (c), the region of highest amplitude in the jet is located in the sixth cell, around $z = 16r_0$, for $St_1 = 0.28$ and in the fifth cell, around $z = 14r_0$, for $St_2 = 0.305$. This result suggests that two different loops establish for the aeroacoustic feedback mechanism, yielding the two screech tones.

In Figure 15(b) and (d), 180° phase shifts with respect to the jet axis are visible. The tone frequencies at $St_1 = 0.28$ and $St_2 = 0.305$ are thus associated with sinuous or helical oscillation modes of the jet. More precisely, using a Fourier decomposition of the fluctuating pressure on 32 sensors regularly spaced in the azimuthal direction, at $z = 0$ and $r = 2r_0$, the two tones appear to be linked to helical oscillation modes. Besides, the amplitude fields in Figure 15(a) and (c) show a strong reduction of the amplitude near the jet axis, as expected for helical modes. In order to visualize these modes, the normalized azimuthal distributions of the fluctuating pressure filtered around the two screech tone frequencies at three times separated $T_s/3$, where $T_s$ is the associated period, are represented in Figure 17. The helical evolution of the fluctuating pressure at the two frequencies is clearly visible. Moreover, the azimuthal distributions are represented at a reference time $T_0$ in black, at $T_0 + T_s/3$ in red

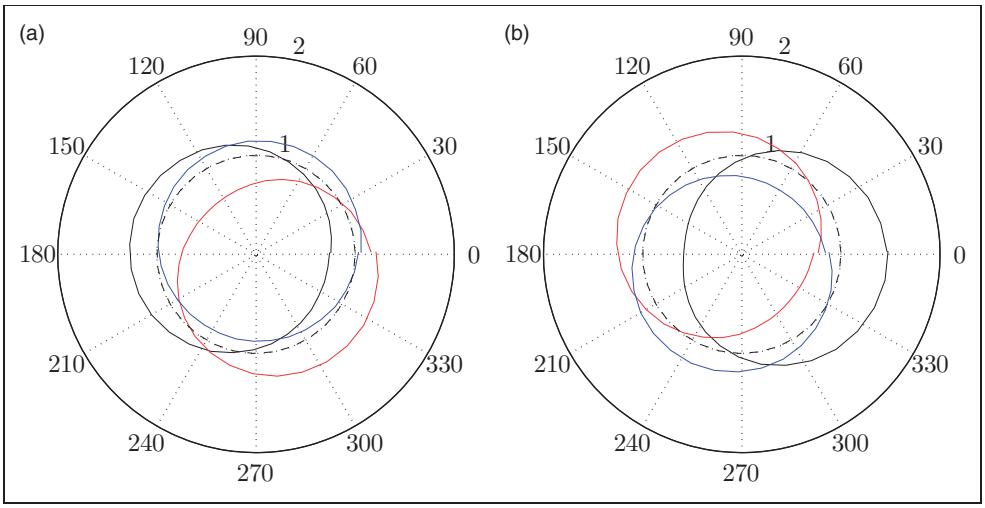


**Figure 17.** Normalized azimuthal distributions of the fluctuating pressure at $z = 0$ and $r = 2r_0$ (a) filtered around $St_1 = 0.28$ at three times separated by $T_1/3$ and (b) filtered around $St_2 = 0.305$ at three times separated by $T_2/3$; – – – unit circle.

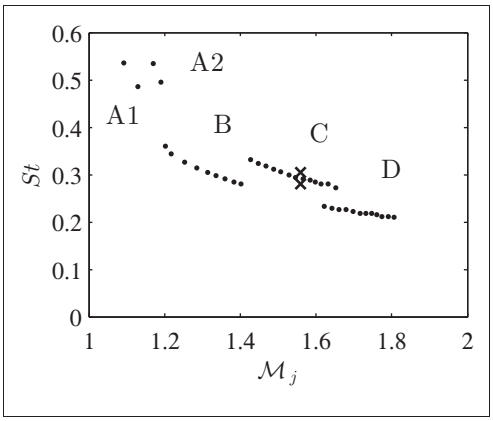


**Figure 18.** Screech tone frequencies obtained • in the experiments of Powell et al.[47] and × in the present jet as a function of the fully expanded Mach number $\mathcal{M}_j$.

and at $T_0 + 2T_s/3$ in blue. This indicates that the two screech tones are associated with anticlockwise helical oscillation modes.

Finally, the screech tone frequencies obtained for the present jet are compared in Figure 18 with the dominant screech tones found in the experiments of Powell et al.[47] for round supersonic underexpanded jets. The experimental tones are associated with axisymmetric oscillation modes $A1$ and $A2$, with sinuous and sometimes helical oscillation modes $B$, with helical oscillation modes $C$, and with sinuous oscillation modes $D$. The screech tone frequencies in the LES fall in the vicinity of the frequencies of tones $C$, in agreement with the

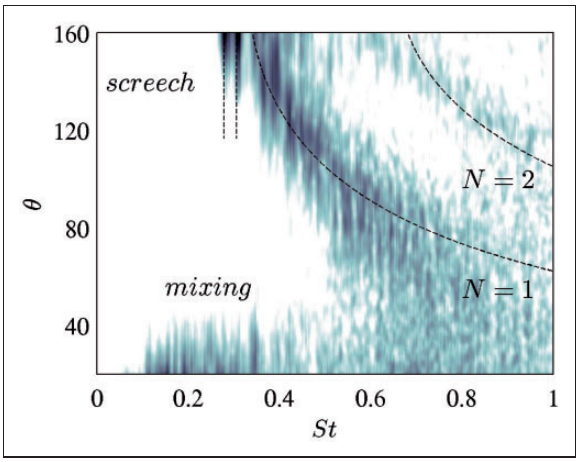


**Figure 19.** Sound pressure levels on the circle centered on the jet axis at $z = 15r_0$, radius $15r_0$, as a function of the Strouhal number and of the angle $\theta$ with respect to the downstream direction.

helical nature reported above. Consequently, both the frequencies of the screech tones and the associated oscillation modes are consistent with the predictions of Panda[41] and the measurements of Powell et al.[47]

## *Fluctuating pressure analysis in the near acoustic field*

The Fourier transform applied to the pressure fields also provides the sound pressure levels in each point of the $(z, r)$ plane. The levels obtained along the circle centered on the jet axis at $z = 15r_0$, radius $15r_0$, are represented in Figure 19 as a function of the Strouhal number and of the angle $\theta$ with respect to the downstream direction.

Several acoustic components typical of non-ideally expanded supersonic jets can be seen in Figure 19. In the upstream direction, for $\theta > 140°$, the screech tone frequencies at $St_1 = 0.28$ and $St_2 = 0.305$ dominate, as previously observed in the pressure spectrum of Figure 13. A second acoustic component is the mixing noise, which is most likely due to two different generation mechanisms.[48–50] In the downstream direction, between $\theta = 20$ and $\theta = 40°$, the mixing noise generated by large scale turbulent structures appears, around a Strouhal number of 0.25. The direction and frequency of this acoustic component are in good agreement with the numerical results of Berland et al.[6] for a planar supersonic jet with $\mathcal{M}_j = 1.55$ and $Re_j = 6 \times 10^4$. In the sideline direction, between $\theta = 50$ and $\theta = 90°$, high-frequency mixing noise can be seen in Figure 19 with a high-amplitude region for $St > 0.5$. The direction of propagation and the broadband spectrum signature are in agreement with the experimental results of Viswanathan.[49] A third acoustic component is visible for $80 < \theta < 160°$. It is characterized by a central frequency which varies with the angle $\theta$. This component is associated with broadband shock-associated noise, as observed in experimental[12–14] and numerical[6,51] studies. A mechanism was proposed by Harper-Bourne and Fisher[15] for this acoustic component. In this mechanism, the broadband shock-associated noise is generated by the interactions between the turbulent structures propagating downstream in the jet shear layers and the shocks of the quasi-periodic shock cell structure.

Each interaction is considered as an acoustic source. The directivity of constructive interference is then determined. This model yields a central frequency

$$f_{shock} = \frac{Nu_c}{L_s(1 - \mathcal{M}_c \cos(\theta))} \tag{9}$$

where $N$ is the mode number, $L_s$ is a length scale related to the shock cell size, and $\mathcal{M}_c = u_c/c_{amb}$ is the convection Mach number. As the cell length varies with the axial direction, as observed in the Mean fields section, it is difficult to choose the value of $L_s$. For screeching jets, Tam et al.[13] suggested that the central frequency of the first mode $N=1$ of the broadband shock-associated noise tends to the screech frequency at $\theta=180°$. Considering equation (8), the length scale $L_s$ in equation (9) can therefore be replaced by the wavelengths of the standing waves $L_{sw}$. Unfortunately, the screech frequencies predicted in this way using the two wavelengths $L_{sw} = 2.85r_0$ and $L_{sw} = 2.6r_0$ found in the Fluctuating pressure in the jet section are not in good agreement with the LES results. Harper-Bourne and Fisher[15] proposed a mean length of $L_s = 1.1\beta D_j = 2.9r_0$ for the shock cell structure but the comparison with the LES results was again not satisfactory. Finally, the size of the sixth shock cell, $Ls_6 = 2.35r_0$, located around $z = 15r_0$, is used in the relation (9) to compute the central frequency of the broadband shock-associated noise as a function of angle $\theta$. The frequencies of the modes $N=1$ and $N=2$ thus obtained are plotted in Figure 19. There is a good agreement with numerical results. One can finally note that in the upstream direction, the relation (9) tends to $St=0.33$. This tone can be observed in the spectrum of Figure 13 at a magnitude of 147 dB, comforting the choice of this length scale.

### *Mixing noise*

The high-frequency mixing noise cannot be studied from amplitude and phase fields at specific frequencies given the large-frequency bandwidth of this noise component. On the contrary, the low-frequency mixing noise generated by the large-scale turbulent structures has a central frequency of about $St=0.25$, and can therefore be examined using a Fourier decomposition of the pressure fields. The amplitude field of the fluctuating pressure obtained at the frequency $St=0.25$ is represented in Figure 20. In the jet, the regions of highest

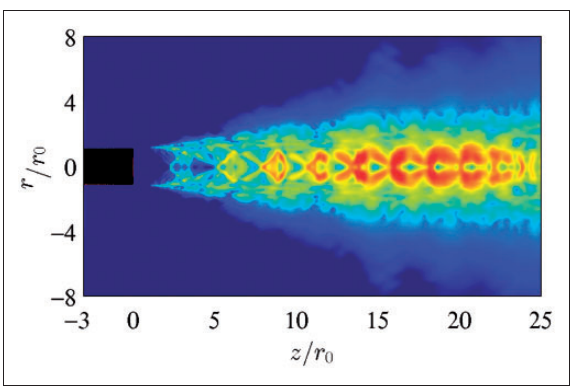


**Figure 20.** Amplitude field of the pressure fluctuations obtained in the (*z*, *r*) plane at the frequency $St=0.25$.

amplitude are located in the sixth cell, around $z = 15r_0$. Therefore, the mixing noise seems to be produced at the end of the potential core, as observed by Bogey and Baily,[7] Sandham and Salgado[8] and Tam[9] for instance.

The Skewness and the Kurtosis factors of the density fluctuations were calculated in the in the $(z, r)$ plane and on the jet axis. These factors are represented in Figure 21. The skewness factor, in Figure 21(a) and (c), remains close to 0 on the jet axis up to the sixth shock cell, with values $S \simeq -1$ found at $z = 14.5r_0$. The kurtosis factor, in Figure 21(b) and (d), in the region near the jet axis is close to $K = 3$ up to the sixth shock cell, where $K \simeq 4$ at $z = 14.5r_0$. These results indicate that large density deficits appear intermittently on the jet axis in the sixth cell, near the end of the potential core. Therefore, the mixing noise seems due to the sudden intrusion of turbulent structures, of low density compared to the exit density, in the potential core, as suggested by Bogey and Baily[7] for subsonic jets and by Cacqueray and Bogey[52] for an overexpanded jet with an ideally expanded Mach number of $\mathcal{M}_j = 3.3$.

### *Broadband shock-associated noise*

In order to investigate the broadband shock-associated noise, the amplitude fields of the pressure fluctuations obtained in the $(z, r)$ plane for frequencies $St = 0.28$, 0.40, 0.50 and 0.60

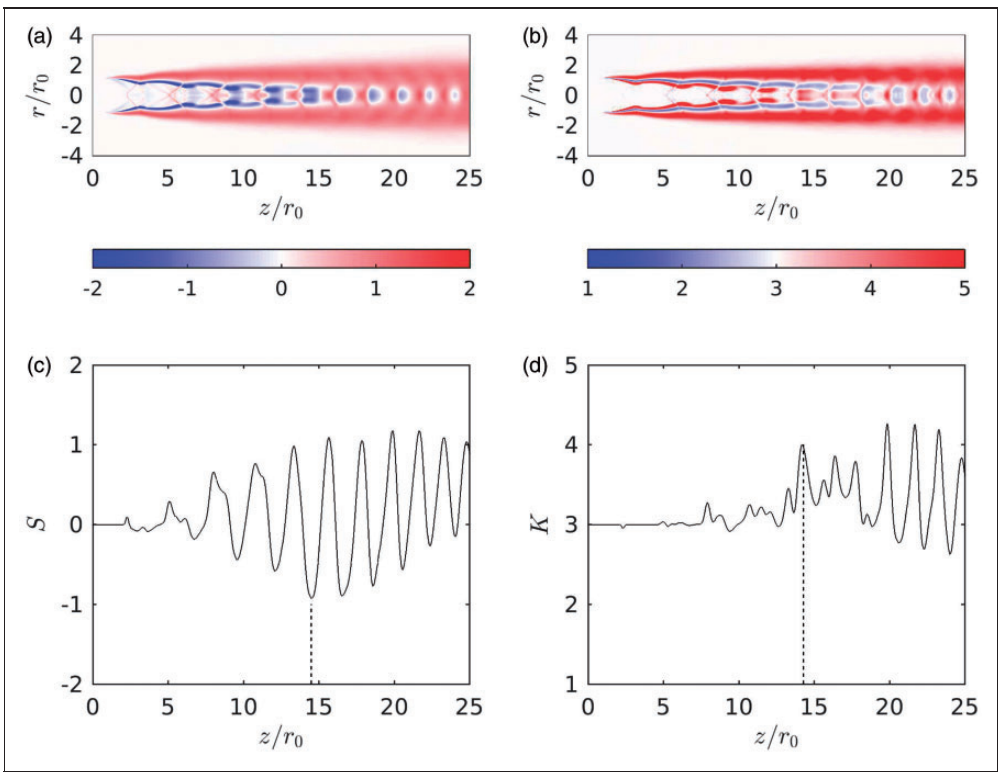


**Figure 21.** (a, c) Skewness and (b, d) kurtosis factors of the density fluctuations obtained (a, b) in the $(z, r)$ plane and (c, d) on the jet axis. The dotted line represent the middle of the sixth shock cell, at $z = 14.5r_0$.

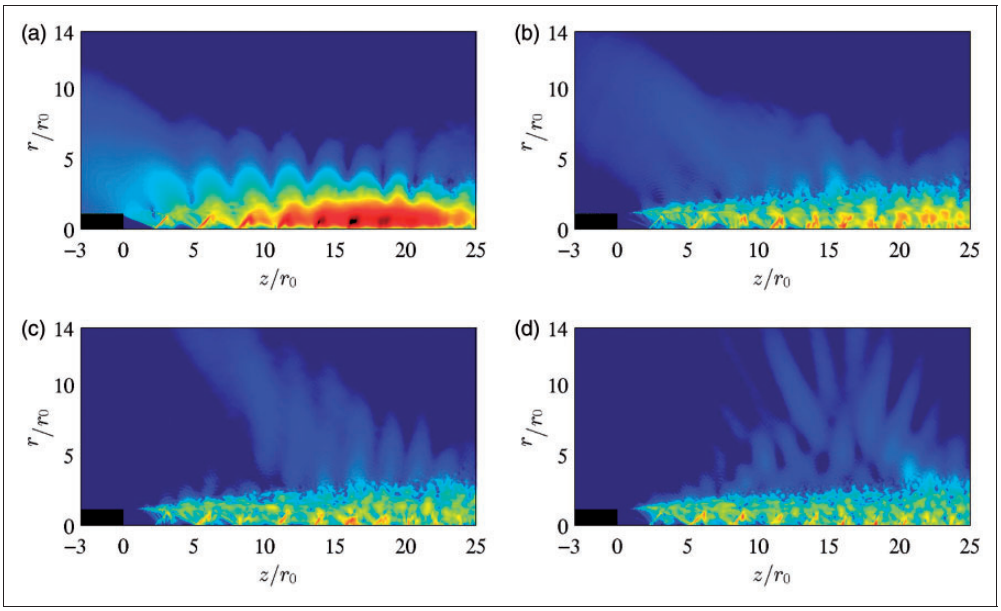


**Figure 22.** Amplitude fields of the pressure fluctuations obtained in the (z, r) plane at the frequencies (a) $St = 0.28$, (b) $St = 0.40$, (c) $St = 0.50$, and (d) $St = 0.60$.

are represented in Figure 22. The first frequency corresponds to the lower screech tone frequency. In the amplitude field at $St = 0.40$, in Figure 22(b), a region of high amplitude is visible at $\theta \simeq 130°$. This contribution can be associated with the direction of constructive interferences of the broadband shock-associated noise. This direction is in good agreement with the value of 125° found for a frequency $St = 0.40$ using equation (9). In the amplitude field at $St = 0.50$, in Figure 22(c), a marked directivity is noted at $\theta \simeq 110°$. Again, this result agrees well with the angle of 104° found at $St = 0.50$ using equation (9). Finally, the amplitude field at $St = 0.60$, in Figure 22(d), does not exhibit a clear directivity, but regions of high amplitude appear in the radial direction. Moreover, at $St = 0.60$, equation (9) leads to an angle of $\theta = 90°$. Furthermore, in Figure 22(b) to (d), in the jet, the regions of highest amplitude are located in the sixth cell, around $z = 15r_0$. This result suggests that the broadband shock-associated noise is produced mainly in the sixth shock cell, at $z \simeq 15r_0$. Therefore, it seems that the constructive interference which produces the broadband shock-associated noise happens mainly between the turbulent structures in the jet shear layers and the shocks of the sixth shock cell. This result enforces the use of the size if this shock cell in the Fluctuating pressure analysis in the near acoustic field section as the length scale in the model of Harper-Bourne and Fisher.[15]

## Conclusion

In this paper, the flow and near pressure fields of an underexpanded supersonic jet have been described. The jet corresponds to the reference jet considered in previous studies. It is characterized by a fully expanded Mach number of 1.56, a Reynolds number of $6 \times 10^4$ and an exit Mach number of 1. Flow snapshots of vorticity, density and pressure as well

as mean velocity fields are shown. The results, including the shock-cell structure, are consistent with experimental data, empirical and theoretical models. The convection velocity of large-scale structures in the jet shear layers is evaluated, and values similar to experimental data are found. The near acoustic pressure fields are then analyzed. Two tone frequencies associated with screech noise are obtained in the acoustic spectrum calculated in the vicinity of the nozzle. Hydrodynamic-acoustic standing waves, typical of this noise component, are observed. The two screech tones are found to be associated with anticlockwise helical oscillation modes. Moreover, a temporal switch between the two screech tone frequencies is noted. Then in the near pressure fields, the low-frequency mixing noise, the high-frequency mixing noise and the broadband shock-associated noise are identified. They are found to be produced mainly in the sixth shock cell. The mixing noise component seems due to the sudden intrusion of turbulent structures into the potential core, near its end. The broadband shock-associated noise appears to originate from the interactions between the turbulent structures in the jet shear layers and the shocks of the sixth shock cell. The use of the size of this shock cell in the classical theoretical model of this noise component is proposed and a good agreement is found with simulation results.

## Acknowledgements

This work was granted access to the HPC resources of FLMSN (Fédération Lyonnaise de Modélisation et Sciences Numériques), partner of EQUIPEX EQUIP@MESO, and of CINES (Centre Informatique National de l'Enseignement Supérieur), and IDRIS (Institut du Développement et des Ressources en Informatique Scientifique) under the allocation 2016-2a0204 made by GENCI (Grand Equipement National de Calcul Intensif).

## Declaration of conflicting interests

The author(s) declared no potential conflicts of interest with respect to the research, authorship, and/or publication of this article.

## Funding

The author(s) disclosed receipt of the following financial support for the research, authorship, and/or publication of this article: This work was performed within the framework of the Labex CeLyA of Université de Lyon, operated by the French National Research Agency (grant no. ANR-10-LABX-0060/ANR-11-IDEX-0007).

## References

1. Powell A. On the mechanism of choked jet noise. *Proc Physical Soc Sect B* 1953; 66: 1039–1056.
2. Raman G. Supersonic jet screech: half-century from Powell to the present. *J Sound Vib* 1999; 225: 543–571.
3. Merle M. Sur la fréquence des ondes sonores émises par un jet d'air a grande vitesse. *Comptes-Rendus de l'Académie des Sciences de Paris* 1956; 243: 490–493.
4. Davies MG and Oldfield DES. Tones from a choked axisymmetric jet. ii. the self excited loop and mode of oscillation. *Acta Acust United Acust* 1962; 12: 267–277.
5. Bogey C and Bailly C. Investigation of downstream and sideline subsonic jet noise using large eddy simulation. *Theor Comput Fluid Dyn* 2006; 20: 23–40.
6. Berland J, Bogey C and Bailly C. Numerical study of screech generation in a planar supersonic jet. *Phys Fluids* 2007; 19: 075105.

7. Bogey C and Bailly C. An analysis of the correlations between the turbulent flow and the sound pressure fields of subsonic jets. *J Fluid Mech* 2007; 583: 71–97.
8. Sandham ND and Salgado AM. Nonlinear interaction model of subsonic jet noise. *Phil Trans R Soc A* 2008; 366: 2745–2760.
9. Tam CKW. Mach wave radiation from high-speed jets. *AIAA J* 2009; 47: 2440–2448.
10. Bogey C, Bailly C and Juvé D. Noise investigation of a high subsonic, moderate reynolds number jet using a compressible large eddy simulation. *Theoret Comput Fluid Dynam* 2003; 16: 273–297.
11. Martlew DL. Noise associated with shock waves in supersonic jets. Aircraft engine noise and sonic boom. *AGARD C.P*. 1969; 42: 1–70.
12. André B. *Etude expérimentale de l'effet du vol sur le bruit de choc de jets supersoniques sous-détendus*. PhD Thesis, Ecole Centrale de Lyon, NNT: 2012ECDL0042, 2012.
13. Tam C.K.W., Seiner J.M. and Yu J.C.. Proposed relationship between broadband shock associated noise and screech tones. *J. Sound Vib*. 1986; 110(2): 309–321.
14. Tam CKW and Tanna HK. Shock associated noise of supersonic jets from convergent-divergent nozzles. *J Sound Vib* 1982; 81: 337–358.
15. Harper-Bourne M and Fisher MJ. The noise from shock waves in supersonic jets. *AGARD CP* 1974; 131: 1–13.
16. Gojon R and Bogey C. Flow structure oscillations and tone production in underexpanded impinging round jets. *AIAA J* 2017; 55: 1–14.
17. Castelain T, Gojon R, Mercier B, et al. Estimation of convection speed in underexpanded jets from schlieren pictures. *AIAA Paper* 2016; 2016–2984: 1–14.
18. Henderson B, Bridges J and Wernet M. An experimental study of the oscillatory flow structure of tone-producing supersonic impinging jets. *J Fluid Mech* 2005; 542: 115–137.
19. Bogey C, Marsden O and Bailly C. Large-eddy simulation of the flow and acoustic fields of a Reynolds number 105 subsonic jet with tripped exit boundary layers. *Phys Fluid* 2011; 23: 1–20.
20. Bogey C and Bailly C. A family of low dispersive and low dissipative explicit schemes for flow and noise computations. *J Comput Phys* 2004; 194: 194–214.
21. Berland J, Bogey C, Marsden O, et al. High-order, low dispersive and low dissipative explicit schemes for multiple-scale and boundary problems. *J Comput Phys* 2007; 224: 637–662.
22. Bogey C and Bailly C. Large eddy simulations of transitional round jets: influence of the Reynolds number on flow development and energy dissipation. *Phys Fluid* 2006; 18: 1–14.
23. Bogey C and Bailly C. Turbulence and energy budget in a self-preserving round jet: direct evaluation using large eddy simulation. *J Fluid Mech* 2009; 627: 129–160.
24. Fauconnier D, Bogey C and Dick E. On the performance of relaxation filtering for large-eddy simulation. *J Turbul* 2013; 14: 22–49.
25. Kremer F and Bogey C. Large-eddy simulation of turbulent channel flow using relaxation filtering: Resolution requirement and Reynolds number effects. *Comput Fluid* 2015; 116: 17–28.
26. Tam CKW and Dong Z. Wall boundary conditions for high-order finite-difference schemes in computational aeroacoustics. *Theor Comput Fluid Dynam* 1994; 6: 303–322.
27. Bogey C, de Cacqueray N and Bailly C. Finite differences for coarse azimuthal discretization and for reduction of effective resolution near origin of cylindrical flow equations. *J Comput Phys* 2011; 230: 1134–1146.
28. Mohseni K and Colonius T. Numerical treatment of polar coordinate singularities. *J Comput Phys* 2000; 157: 787–795.
29. Bogey C, de Cacqueray N and Bailly C. A shock-capturing methodology based on adaptative spatial filtering for high-order non-linear computations. *J Comput Phys* 2009; 228: 1447–1465.
30. de Cacqueray N, Bogey C and Bailly C. Investigation of a high-mach-number overexpanded jet using large-eddy simulation. *AIAA J* 2011; 49: 2171–2182.
31. Arnette SA, Samimy M and Elliott GS. On streamwise vortices in high Reynolds number supersonic axisymmetric jets. *Phys Fluids* 1993; 5: 187–202.

32. Lau JC, Morris PJ and Fisher MJ. Measurements in subsonic and supersonic free jets using a laser velocimeter. *J Fluid Mech* 1979; 93: 1–27.
33. Tam CKW, Jackson JA and Seiner JM. A multiple-scales model of the shock-cell structure of imperfectly expanded supersonic jets. *J Fluid Mech* 1985; 153: 123–149.
34. Powell A. The sound-producing oscillations of round underexpanded jets impinging on normal plates. *J Acoust Soc Am* 1988; 83: 515–533.
35. Henderson B. The connection between sound production and jet structure of the supersonic impinging jet. *J Acoust Soc Am* 2002; 111: 735–747.
36. Addy AL. Effects of axisymmetric sonic nozzle geometry on mach disk characteristics. *AIAA J* 1981; 19: 121–122.
37. André B, Castelain T and Bailly C. Investigation of the mixing layer of underexpanded supersonic jets by particle image velocimetry. *Intl J Heat Fluid Flow* 2014; 50: 188–200.
38. Prandtl L. Uber die stationren wellen in einem gasstrahl. *Physikalische Zeitschrift* 1904; 5: 599–601.
39. Pack DC. A note on Prandtl's formula for the wave-length of a supersonic gas jet. *Q J Mech Appl Math* 1950; 3: 173–181.
40. Westley R and Woolley JH. The near field sound pressures of a choked jet during a screech cycle. *AGARD CP* 1969; 42: 1–23.
41. Panda J. An experimental investigation of screech noise generation. *J Fluid Mech* 1999; 378: 71–96.
42. Raman G. Cessation of screech in underexpanded jets. *J Fluid Mech* 1997; 336: 69–90.
43. Raman G. Screech tones from rectangular jets with spanwise oblique shock-cell structures. *J. Fluid Mech* 1997; 330: 141–168.
44. Gojon R and Bogey C. On the oscillation modes in screeching jets. *AIAA J* 2017; submitted.
45. Gojon R, Bogey C and Marsden O. Investigation of tone generation in ideally expanded supersonic planar impinging jets using large-eddy simulation. *J Fluid Mech* 2016; 808: 90–115.
46. Bogey C and Gojon R. Feedback loop and upwind-propagating waves in ideally-expanded supersonic impinging round jets. *J Fluid Mech* 2017; 823: 562–591.
47. Powell A, Umeda Y and Ishii R. Observations of the oscillation modes of choked circular jets. *J Acoust Soc Am* 1992; 92: 2823–2836.
48. Tam CKW, Golebiowski M and Seiner JM. On the two components of turbulent mixing noise from supersonic jets. *AIAA Paper* 1996; 1996–1716: 1–11.
49. Viswanathan K. Analysis of the two similarity components of turbulent mixing noise. *AIAA J* 2002; 40: 1735–1744.
50. Tam CKW, Viswanathan K, Ahuja KK, et al. The sources of jet noise: experimental evidence. *J Fluid Mech* 2008; 615: 253–292.
51. Dahl MD. Predictions of supersonic jet mixing and shock-associated noise compared with measured far-field data. *NASA Technical Report*, TM-2010-216328, 2010.
52. de Cacqueray N and Bogey C. Noise of an overexpanded mach 3.3 jet: non-linear propagation effects and correlations with flow. *Int J Aeroacoust* 2014; 13: 607–632.